New insights into lunar petrology: Distribution and composition of prominent low-Ca pyroxene exposures as observed by the Moon Mineralogy Mapper (M^3)

Rachel L. Klima,[1] Carle M. Pieters,[2] Joseph W. Boardman,[3] Robert O. Green,[4] James W. Head III,[2] Peter J. Isaacson,[2] John F. Mustard,[2] Jeff W. Nettles,[2] Noah E. Petro,[5] Matthew I. Staid,[6] Jessica M. Sunshine,[7] Lawrence A. Taylor,[8] and Stefanie Tompkins[9]

Received 24 August 2010; revised 19 January 2011; accepted 31 January 2011; published 14 April 2011.

[1] Lunar geochemical groups such as Mg suite, ferroan anorthosite, and alkali suite rocks are difficult to distinguish from orbit because they are defined by both modal mineralogy and elemental composition of their constituent minerals. While modal mineralogy can be modeled, only specific minerals or elements can be directly detected. At near-infrared (NIR) wavelengths, pyroxenes are among the most spectrally distinctive minerals, and their absorption bands are sensitive to structure and composition. Pyroxenes thus provide important clues to distinguish these geochemical groups and to understand lunar crustal evolution. Using Moon Mineralogy Mapper data, we search for lithologies dominated by strong low-calcium pyroxene (LCP) signatures. We compare the NIR absorptions of 20 LCPs to a suite of synthetic pyroxenes to determine which lunar pyroxenes appear magnesian enough to be candidate Mg suite norites. We detail three prominent regions of LCP (1) in South Pole–Aitken Basin (SPA), (2) south of Mare Frigoris, and (3) north of Mare Frigoris. The absorption band positions suggest that the LCPs north of Mare Frigoris and those in SPA are compositionally similar to one another and of ~$Mg_{50–75}$, implying that the mafic material excavated by the SPA impact was relatively iron-rich. Modified Gaussian modeling results suggest that the Apollo basin may have tapped different composition material than is exposed in much of SPA. The LCPs located in the highlands south of Mare Frigoris exhibit absorption bands at short wavelengths consistent with Mg > ~80. The coincidence of these Mg-rich LCPs with the thorium measured by Lunar Prospector make them good candidates for KREEP-related Mg suite pyroxenes.

Citation: Klima, R. L., et al. (2011), New insights into lunar petrology: Distribution and composition of prominent low-Ca pyroxene exposures as observed by the Moon Mineralogy Mapper (M^3), *J. Geophys. Res.*, *116*, E00G06, doi:10.1029/2010JE003719.

1. Introduction

[2] Pyroxenes are the dominant mafic minerals on the lunar surface, and are readily observed in returned samples, lunar meteorites, and remote measurements. In their crystal structure and composition, pyroxenes capture information about their magmatic source and cooling history, some of which is directly reflected in their spectral properties. It has thus been the goal of much spectroscopic research to develop pyroxene spectroscopy as a tool to assess the composition [e.g., *Adams*, 1974; *Cloutis and Gaffey*, 1991; *Sunshine and Pieters*, 1993; *Klima et al.*, 2007, 2011] and geothermometry [e.g., *Cloutis and Gaffey*, 1991; *Klima et al.*, 2008; *Cloutis et al.*, 2010] of remotely observed surfaces.

[3] Pyroxenes provide important clues for understanding the evolution of the lunar surface, from the earliest magma ocean cumulates, through the anorthositic flotation crust, to later stage intrusive and extrusive magmatism. Though the lunar samples have enabled detailed petrographic and compositional analyses, the majority of regolith samples are brecciated mixtures of clasts from across the lunar surface. Without remote sensing, there would be no way to put the samples into a global perspective. Fortunately, broad lithologies such as the mare basalts and highland anorthosites are easily identifiable, both telescopically and from orbit.

[1]Johns Hopkins University Applied Physics Laboratory, Laurel, Maryland, USA.
[2]Department of Geological Sciences, Brown University, Providence, Rhode Island, USA.
[3]Analytical Imaging and Geophysics LLC, Boulder, Colorado, USA.
[4]Jet Propulsion Laboratory, Pasadena, California, USA.
[5]NASA Goddard Space Flight Center, Greenbelt, Maryland, USA.
[6]Planetary Sciences Institute, Tucson, Arizona, USA.
[7]Department of Astronomy, University of Maryland, College Park, Maryland, USA.
[8]Planetary Geosciences Institute, University of Tennessee, Knoxville, Tennessee, USA.
[9]Defense Advanced Research Projects Agency, Arlington, Virginia, USA.

Copyright 2011 by the American Geophysical Union.
0148-0227/11/2010JE003719

However, more specific geochemical groups, such as the Mg suite highlands rocks and chemical groups within mare basalts, are more difficult to distinguish.

[4] The Clementine mission to the Moon enabled mapping of general pyroxene mineralogies on the lunar surface. Though much of the Moon is covered by a mature regolith, the central peaks of many impact craters generally remain less affected by space weathering due to their relative youth and steep physical slopes and are more likely to represent the local bedrock at depth. *Tompkins and Pieters* [1999] mapped the distribution of spectral classes across the Moon by analyzing Clementine UVVIS spectra of the central peaks of 109 impact craters ranging from 40 to 180 km in diameter. Their findings suggested that the lunar crust is compositionally diverse, with pyroxene-bearing lithologies ranging from gabbroic through noritic. The majority of pyroxenes (mostly clinopyroxenes) occur in the basalts in the maria, although norites, gabbronorites, and gabbros are found throughout the highlands in association with varying amounts of anorthite-rich plagioclase.

[5] Evidence from laboratory studies of lunar rocks combined with that of telescopic and orbital remote sensing studies support the Lunar Magma Ocean (LMO) hypothesis for the early thermal evolution of the Moon [e.g., *Wood et al.*, 1970; *Shearer et al.*, 2006]. In this model, the cooling LMO first crystallized magnesium-rich mafic minerals (olivine, orthopyroxene), which settled toward the lunar interior. As crystallization continued, the residual liquid and the accumulating mafics became increasingly more Fe-rich. Once plagioclase began to crystallize, it, being less dense than the residual liquid, floated to the surface to form the primary lunar crust. Originally sandwiched between the mafic cumulate pile and the feldspathic crust was the dense, iron and incompatible element-rich layer of late stage residual liquid (potassium, rare earth element, and phosphorus (KREEP)) and Fe-rich cumulates such as ilmenite. It is interpreted this gravitationally unstable arrangement of a cumulate pile consisting of Mg-rich mafic minerals underlying Fe-rich minerals would result in dynamic overturn, dragging some of the heat producing elements deeper into the lunar interior and helping to fuel secondary melting [e.g., *Ryder*, 1991; *Shearer et al.*, 2006]. Regardless of the efficiency of overturn, the primary lunar crust is expected to be generally anorthositic at the surface, becoming more noritic or gabbroic at depth [e.g., *Ryder and Wood*, 1977; *Warren*, 1985, 1990; *Hess and Parmentier*, 1995; *Shearer and Papike*, 2005].

[6] Mg suite rocks, which have been studied in detail in lunar samples, are hypothesized to be mafic intrusions emplaced within the resulting anorthositic crust. The complex geochemistry of the Mg suite rocks has been explained by differing amounts of assimilation and mixing of KREEP and anorthositic crust with a magma derived from either the primitive lunar mantle or the LMO cumulate pile [e.g., *Shearer et al.*, 2006]. The Mg suite remains enigmatic, and a better understanding of the geographic distribution and compositions of Mg-rich lithologies on the lunar surface would provide valuable constraints on petrogenetic models for intrusive post-LMO lunar magmatism.

[7] On the basis of Clementine and Lunar Prospector data, *Jolliff et al.* [2000] suggested that the Mg suite is associated only with the Procellarum KREEP Terrane (PKT), which encompasses most of the nearside maria [*Wieczorek and Phillips*, 2000]. More recently, candidate Mg suite locations were identified using radiative transfer modeling of Clementine data [*Cahill and Lucey*, 2007; *Lucey and Cahill*, 2009], including a number of sites outside of the PKT. Though the multispectral imaging capabilities of Clementine revolutionized global mineralogical mapping of the Moon, a higher spectral and spatial resolution is necessary to reduce the uncertainties in remotely estimating iron/magnesium ratios within mafic minerals of compositionally distinct mare basalt and/or highland deposits. The Moon Mineralogy Mapper (M^3), flown on Chandrayaan-1, was designed specifically for this purpose. M^3, a visible-infrared imaging spectrometer, imaged the surface of the Moon at 140 m/pixel using 85 spectral channels from approximately 400–3000 nm in its low-resolution global mode with selected observations at higher spatial and spectral resolution [e.g., *Pieters et al.*, 2009; R. O. Green et al., The Moon Mineralogy Mapper (M3) imaging spectrometer for lunar science: Instrument, calibration, and on-orbit measurement performance, submitted to *Journal of Geophysical Research*, 2011]. These data provide an opportunity to examine pyroxene compositions across the lunar surface in detail. Our primary goal in this work is to search for lithologies dominated by strong low-calcium (Wo < 15) pyroxene spectral signatures. We then examine in more detail the absorption bands of 20 regions in which we have detected strong spectral signatures of low-Ca pyroxene to determine which, if any, of the norites are likely to be compositionally similar to Mg suite norites and which are likely to be norites or noritic anorthosites from the ferroan anorthosite (FAN) suite.

2. Background

2.1. Pyroxenes in Lunar Samples

[8] Pyroxene represents the major mafic mineral in mare basalts, occurring in low-calcium pigeonite, orthopyroxene, and high-calcium augite forms. In many cases, single pyroxene grains are extensively zoned, with more magnesian pigeonite cores grading into more ferrous, higher-calcium augite at the rims. The Mg number (Mg # = molar Mg/(Mg + Fe)*100) of pigeonite is typically around Mg_{65}, with the augite commonly having much lower Mg # of 20 or lower, a product of extreme fractional crystallization [e.g., *Heiken et al.*, 1991].

[9] Orthopyroxene in highland FAN suite rocks is dominantly iron-rich. Pyroxene grains are a volumetrically minor component of FAN (~5–10 vol. %), but because of the transparency of plagioclase in the near-infrared, they are readily identifiable using orbital or telescopic reflectance spectroscopy. The textures of FAN pyroxenes, especially inversion of orthopyroxene from clinopyroxene, suggest slower cooling than the mare basalts. It is likely that in most cases, these grains represent pigeonite that transformed to orthopyroxene and augite upon cooling. The Mg # of the pyroxene grains in the FAN suite are variable, though the majority range from about Mg # 55–75 [e.g., *Heiken et al.*, 1991; *Cahill and Lucey*, 2007].

[10] Pyroxene grains in Mg suite rocks are also coarse grained and texturally indicative of slow cooling. However, in this case it is thought that the orthopyroxenes are directly crystallized from a liquid, rather than products of pigeonite inversion [e.g., *Heiken et al.*, 1991]. As suggested by the

name, Mg suite pyroxenes are the most magnesian of lunar pyroxenes, with Mg # clustering around 80.

2.2. Pyroxene Spectroscopy

[11] Pyroxene can belong to either the orthorhombic (ortho) or monoclinic (clino) symmetry groups. Both orthopyroxenes and clinopyroxenes have two nominally octahedral cation sites, M1 and M2. These sites are coordinated with between 6 and 8 nearest-neighbor oxygens, depending on the crystallographic structure of the pyroxene. The M2 site is larger than the M1 site, and its geometry is more distorted. These crystallographic properties result in the major (Ca^{2+}, Mg^{2+}, and Fe^{2+}) and minor (e.g., Al^{3+}, $Ti^{3+/4+}$, etc.) cations partitioning more favorably into one site or the other based on their size and charge. For cations of similar charge, such as Mg^{2+} and Fe^{2+}, the ordering between sites depends on the cooling rate, as well as the bulk composition and structure of the pyroxene. Because of the difference in structure, there cannot be full solid solution throughout the pyroxene mineral series. As a result, most pyroxene crystals exhibit some degree of zoning, exsolution, or inversion, which is also dependent on cooling history. Pyroxene geothermometry and geospeedometry thus involve measuring the compositions of coexisting pyroxenes [e.g., *Lindsley*, 1983] or the ordering of Fe^{2+} between the M1 and M2 sites [e.g., *Virgo and Hafner*, 1970; *Saxena and Ghose*, 1971].

[12] The most prominent near-infrared spectral features of pyroxene are the strong 1 and 2 μm absorption bands. These bands are caused by crystal field transitions, which occur when transition metals with incompletely filled d-orbitals (i.e., Fe^{2+}, Ti^{3+}) reside in a ligand field [*Burns*, 1993]. Minerals that do not contain transition metals are generally spectrally bland in the near infrared, making these wavelengths ideal for studying iron-bearing silicate mineralogy. Electronic transitions of Fe^{2+} in the M2 site dominate most pyroxene spectra, producing the strong absorptions near 1 and 2 μm. Ions of Fe^{2+} in the M1 site result in additional absorptions near 1 and 1.2 μm. The specific energies of these absorptions depend on the structure of the pyroxene and on which cations reside in the M1 and M2 sites. In general, the positions of the 1 and 2 μm absorptions shift to longer wavelengths with increasing Fe^{2+} and Ca^{2+} in the pyroxene. The properties of pyroxene absorption bands are directly dependent on the mineral structure, chemical composition, petrograpic texture (e.g., exsolution, zoning), and grain size. Thus, a pyroxene spectrum is a convolution of many possible variables. Laboratory studies coordinating pyroxene composition with spectral properties [e.g., *Adams*, 1974; *Cloutis and Gaffey*, 1991; *Klima et al.*, 2007, 2011; *Denevi et al.*, 2007] provide the groundwork for extracting compositional and mineralogical information from remotely sensed spectra. For orthopyroxenes, where Ca^{2+} is low, band positions primarily reflect differences in the Mg^{2+}-Fe^{2+} ratio, with the highest-Mg, lowest-Ca pyroxenes exhibiting the shortest 1 and 2 μm band positions. The absorption band positions of middle-high Fe^{2+} orthopyroxenes and low-middle Fe^{2+} pigeonites (clinopyroxenes) overlap one another, making it impossible to uniquely identify a particular crystallographic structure on the basis of the 1 and 2 μm band positions. Throughout this paper, we use the convention of grouping orthopyroxenes and low-Ca clinopyroxenes (pigeonite, clinoenstatite, etc.) under the term "low-Ca pyroxene."

2.3. The Moon Mineralogy Mapper (M^3)

[13] The M^3 spectrometer was a guest instrument on the Chandrayaan-1, the Indian Space Research Organization's (ISRO) first mission to the Moon [*Goswami and Annadurai.*, 2009]. The M^3 was designed to operate in two modes, global and targeted. Full spatial resolution (600 cross-track pixels at 70 m/pixel) and full-spectral resolution (260 bands at 10 nm from ~400 to 3000 nm) targeted data was only obtained for a limited number of locations on the Moon, largely because of the early end of the mission. However, almost the entire lunar surface was imaged in the reduced resolution global mode (140 m/pixel from a 100 km orbit, 280 km/pixel from a 200 km orbit and 85 spectral bands). The M^3 data are calibrated using a combination of preflight and inflight calibration procedures (Green et al., submitted manuscript, 2011). The M^3 level 1B data have also been registered by ray tracing each M^3 spatial element on the lunar surface to a LOLA-derived lunar reference frame [*Boardman et al.*, 2011].

3. Methods

3.1. Global Mapping

[14] An initial survey of the mineralogy of the lunar surface was conducted using a simple cylindrical global mosaic of M^3 data, spatially binned at 10 × 10 pixels (~1.4 km/pixel) for data validation and calibration [*Boardman et al.*, 2011]. The mosaic includes data from optical period 1b, collected early in the mission, covering a large portion of the nearside of the Moon and data from optical period 2a, which spans the Moon from about 150°W to 10°W latitude (Green et al., submitted manuscript, 2011). The spectra within this data set were all acquired in M^3's reduced resolution global mode, with 85 channels, between 20 and 40 nm spectral sampling and 140 m/pixel spatial resolution. The level 1b radiance data (calibration K (see Green et al., submitted manuscript, 2011)) were processed to apparent reflectance by dividing out solar irradiance and performing a cos (i) correction.

[15] Since the goal of this work is to characterize not only the distribution, but also the approximate composition of low-Ca pyroxene, we limited our search to regions with relatively strong 1 and 2 μm absorption bands. Candidate locations were identified primarily by the strength of their continuum-removed band depth at 1900 nm; some dark regions were filtered out because their spectra did not exhibit deep enough absorption bands to confidently model the shapes of the absorption features. To help in identifying regions with exposures that were both bright enough to exhibit strong absorption band, and spectrally dominated by low-Ca pyroxene with little to no high-Ca pyroxene, we used the following algorithm:

$$\text{LCP index} = (R_{1548} < 0.15)*\ 0 + (R_{1548} > 0.15)*(BD_{1900} - BD_{2300}) \quad (1)$$

where R_{1548} is the reflectance at 1548 nm and BD_{1900} and BD_{2300} are the continuum-removed band depths at 1898 nm (continuum at 1408 and 2498 nm) and 2298 nm (continuum at 1598 and 2578 nm), respectively. This index is based on low-Ca pyroxene exhibiting a 2 μm band that is strongest near 1900 nm, and high-Ca pyroxene exhibiting a band at 2300 nm. It should not be interpreted as mapping all low-Ca

exposures, but rather as a tool to identify those exposures with strong absorption bands that are dominated by low-Ca pyroxene and suitable for Modified Gaussian Model (MGM) analysis [*Sunshine et al.*, 1990].

[16] The integrated band depths of the 1 and 2 μm bands were also used to identify areas of interest [see *Mustard et al.*, 2011 for integrated band depth equations]. Though this survey is restricted to large (visible at the 1km/pixel level) outcrops that are relatively unaffected by space weathering and where the spectrally dominant mineral is low-Ca pyroxene, there are numerous other locations on the Moon with weaker noritic signatures, and/or with low-Ca pyroxene found in close association with other mafic minerals. We are not explicitly addressing the amount of plagioclase in any of these exposures, as radiative transfer modeling require a full photometric correction. We do, however, expect that most of the exposures are noritic and few, if any, represent pyroxenite bulk compositions.

[17] Targeting outcrops spectrally dominated by low-Ca pyroxene has at least two advantages. As mentioned previously, it avoids much of the ambiguity involved in relating band position to iron content, since calcium is generally only present in small amounts. Furthermore, since the band positions of orthopyroxenes, particularly enstatite-rich orthopyroxenes, occur at the shortest wavelengths of the pyroxene series, these bands are least likely to be affected by thermal emission from the lunar surface. Nevertheless, thermal emission can begin to be a factor after 2.2 μm on warm lunar surfaces because the short-wavelength tail of the thermal emission blackbody curve begins to overlap with these wavelengths. The thermal emission upturn can be clearly distinguished and removed in soils where the spectrum beyond 2.2 μm is a basically straight slope [*Clark et al.*, 2011]. In pyroxene-bearing targets, the addition of the thermal emission within the pyroxene 2 μm absorption results in anomalous band widths and complicates thermal removal procedures.

3.2. Compositional Analysis

3.2.1. The Modified Gaussian Model

[18] Spectra for each of the locations in this study were modeled using the Modified Gaussian Model (MGM). The MGM is used to deconvolve an individual spectrum into a continuum and a series of modified Gaussian curves that can be attributed to specific electronic absorptions [*Sunshine et al.*, 1990, 1999]. It can also be used to isolate individual pyroxene phases in a composite spectrum of multiple pyroxenes [*Sunshine and Pieters*, 1993]. The MGM was chosen for this study so that band positions could be related to those measured for synthetic pyroxenes [*Klima et al.*, 2007, 2011], lunar soils [*Noble et al.*, 2006], and lunar pyroxenes [*Klima et al.*, 2009]. Modeled band centers for the 1 and 2 μm bands are compared with the band positions for a suite of synthetic orthopyroxenes [*Klima et al.*, 2007] and low-Ca clinopyroxenes [*Klima et al.*, 2011] to evaluate the approximate Mg # range for the pyroxene exposures. Since we seek to identify broad compositional trends and assess whether they are spatially significant, exposures are classified as high (Mg # > 75), medium or moderate (Mg # 50–75), and low (Mg # < 50) magnesium ratio.

[19] Though locations were selected on the basis of being heavily dominated by low-Ca pyroxene, without any obvious high-Ca pyroxene present, many of the 2 μm bands are somewhat broader than expected. This could be caused by thermal emission or by the presence of small amounts of high-Ca pyroxene. Nevertheless, we have chosen to model the locations using the simplified assumption that only one pyroxene is present, so 5–6 bands are used in each fit. This allowed the model to be run without any constraints imposed. Two of the bands are used to describe the metal-oxygen charge transfer edge in the visible, three are used to describe the pyroxene spin-allowed crystal field bands (bands near 1, 1.2 and 2 μm), and the final band is added, when necessary, to account for the OH^- feature near 2.8–3 μm. As described in more detail in section 3.2.2, we tried two options to model the continuum slope: linear in wavelength and linear in wave number. We chose to use a linear wavelength slope for the final fits, as it resulted in less residual error around the absorption bands. Though the modeling here is relatively simplistic, it is sufficient for identifying major differences in low-Ca pyroxene composition. More rigorous modeling of specific locations of interest will be conducted once thermal and proper photometric corrections are in place.

3.2.2. Limitations and Sources of Error

[20] Though having 85 spectral channels is a substantial improvement over previous global data, the changes in band position that we seek to quantify are small relative to the spectral sampling. In the 1 μm region, global M^3 data are sampled every 20 nm, but the total shift in 1 μm band position for orthopyroxenes is only about 40 nm across the full range of Mg^{2+}-Fe^{2+} compositions from enstatite to ferrosilite [e.g., *Klima et al.*, 2007]. We have chosen to use the MGM to identify the band centers near 1 and 2 μm, but because of the spectral sampling, the model has to rely heavily on the edges of the bands to best fit to the data. The choice of continuum thus plays a large part in the final model results for the 1 μm band position. An additional possible source of error near 1 μm is that the K calibration data do not contain a correction for scattered visible light on the detector, influencing the continuum slope of the spectra shortward of 1 μm (Green et al., submitted manuscript, 2011). Near 2 μm, the spectral sampling is 40 nm, but the total difference in band position from an enstatite to a ferrosilite is about 270 nm. In the absence of strong thermal emission, the continuum slope is also easier to define between 1500 and 2600 nm, making the fits near 2 μm less dependent on model inputs and constraints.

[21] Several steps have been taken to quantify the error in the compositional estimates for this project. The M^3 imaged the central peak of Bullialdus during both optical periods 1b and 2a, which had approximately opposite illumination conditions. We evaluate the band positions for data from both optical periods at the same geographic location to test the variability of apparent band position with different lighting and thermal conditions and with the age of the spacecraft and instrument. Spectra from the same location on the side of the northwestern face of the central peak of Bullialdus were extracted from data in both optical periods, and processed to apparent reflectance.

[22] The MGM allows a continuum slope to be fit as either a slope that is linear in wavelength space or linear in energy space. In all spectral modeling, the continuum is a large source of uncertainty. The optical effects of space weathering on lunar soils make fitting a single straight-line continuum (in either wavelength or energy) to a full visible near-infrared

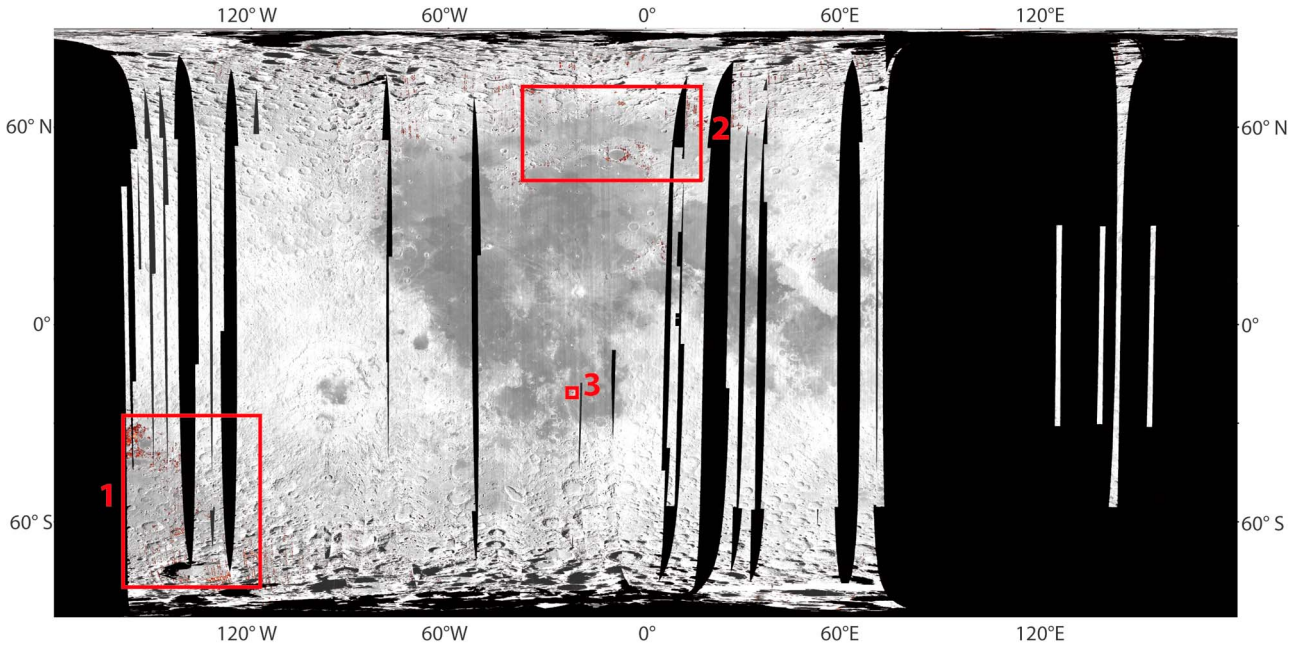

Figure 1. Global 1486 nm reflectance mosaic of optical period 1b and 2a data coverage. Spatial resolution is roughly 1.4 km/pixel (10 × 10 bins of global mode data). Red boxes enclose the three major regions focused on in this work (1) SPA, (2) north and south of Mare Frigoris and (3) the central peak of Bullialdus. The majority of strong low-Ca pyroxene detections are small in lateral extent and thus are not visible at this scale. However, more extensive exposures are shaded in red within boxes 1 and 2.

(NIR) spectrum of lunar soil (laboratory or remotely sensed) inaccurate. In the lab, a continuum that is linear in wavelength near 2 μm and linear in wave number near 1 μm has been relatively effective in describing a weathered soil spectrum using the MGM [*Hiroi et al.*, 2000; *Noble et al.*, 2006]. We tested both linear wavelength and linear energy continua for a range of sites. The 1 and 2 μm pyroxene bands are both dominantly a result of crystal field transitions of Fe^{2+} in the M2 pyroxene site, and thus the energies that these transitions occur at are well-constrained relative to one another [*Adams*, 1974; *Cloutis and Gaffey*, 1991; *Klima et al.*, 2007, 2011]. We can therefore evaluate our fits on the basis of whether the two bands plot within the ranges observed for lunar, terrestrial, and synthetic pyroxenes measured in the lab. It was determined that fits that were performed using a continuum that was linear in wavelength, and approximately parallel to the peak reflectances near 1350 and 2450 nm resulted in the best fits for each location, and thus a continuum that is linear in wavelength is used for all compositional estimates in this work.

[23] Finally, though most of the strong low-Ca pyroxene detections are located outside of the equatorial region, thermal emission is a concern for the apparent position of the 2 μm band. Each site has been fit three times, once with the full spectrum, once with a spectrum that has been truncated at 2.6 μm, and once with a spectrum that has been truncated at 2.2 μm. The band positions reported are an average for the three iterations of fits, which generally only vary on the order of a couple of nm for the 1 μm band, but may vary by 10s of nm for the 2 μm band.

[24] We have carefully chosen our spectra to have very strong low-Ca pyroxene bands, with little to no contribution from high-Ca pyroxene or olivine. Since we fit the spectra using only three crystal field bands (representing a single pyroxene), and the 1 and 2 μm pyroxene bands are well separated from one another (as opposed to overlapping as in olivine) the model is insensitive to the starting band parameters. If a high- and low-Ca pyroxene component were being included in the fits, we would expect more uncertainty in the band positions, as detailed by *Kanner et al.* [2007]. However, we are confident that the M^3 observations selected are dominated by a single pyroxene.

[25] The difference in wavelength between modeled band centers for fits to the M^3 data using all of the different continua, starting band parameters, and thermal cutoffs are included as part of the reported error. Error bars are determined individually for each location. The final uncertainty reported is always at least ±10 nm for all band positions (or known to within a range of 20 nm), even if the difference in band positions for all of the fits was smaller. This is to account for the possible effects of illumination conditions, since only Bullialdus was able to be modeled during different optical periods. In general, the 1 μm band uncertainty is ±10 nm. At 2 μm, the reported error is often larger, ranging from an uncertainty of approximately 20–50 nm.

4. Results

4.1. Global Distribution of Low-Ca Pyroxene on the Moon

[26] Figure 1 is a 1489 nm albedo map of the combined coverage for optical periods 1b and 2a with the locations of the strongest low-Ca pyroxene deposits superimposed. The largest regional deposits of low-Ca pyroxene are focused

Table 1. Craters Selected for Compositional Analyses

Site	Location	Region	Latitude	Longitude	Phase Angle[a]	Mg Range 1 μm[b]	Mg Range 2 μm[c]
1	Dryden	Apollo Basin (SPA)	−33.1	204.6	62	high	high
2	Chaffee S	Apollo Basin (SPA)	−39.8	202.5	66	high	high
3	Chaffee	Apollo Basin (SPA)	−39.2	205.0	62	high	med
4	Minkowski	South Pole Aitken	−56.4	214.0	63	med	low
5	Fizeau	South Pole Aitken	−58.3	226.2	71	med	low
6	Lemaitre F	South Pole Aitken	−61.3	210.0	74	high	low
7	Eijkman	South Pole Aitken	−63.2	217.3	69	med	low
8	Doerfel S	South Pole Aitken	−69.8	239.4	75	med	med
9	Zeeman	South Pole Aitken	−73.9	230.5	74	med	med
10	Vallis Alpes	South of Frigoris	49.2	2.0	55	high	high
11	Plato	South of Frigoris	52.2	354.1	65	high	high
12	Epigenes F	North of Frigoris	67.2	352.6	66	med	low
13	unnamed crater	North of Frigoris	65.3	15.7	71	low	low
14	unnamed crater	North of Frigoris	71.4	351.8	68	med	med
15	Philolaus	North of Frigoris	70.8	324.7	77	high	med
16	La Condamine A	South of Frigoris	54.8	330.1	67	high	high
17	Bouguer	South of Frigoris	52.1	324.2	63	med	high
18	Bullialdus	Low Lat. Nearside	−20.7	337.5	57	high	high
19	Bhabha	South Pole Aitken	−55.1	195.5	55	med	low
20	Moscoviense	Low Lat. Farside	22.1	142.3	42	med	med

[a]Phase angle is for the extracted spectrum without topography taken into account. Phase angle given for sites 19 and 20 is the average phase angle for the strip.
[b]Mg range based on the 1 μm band position: high is defined as roughly Mg # > 75, med ranges from Mg # 50 to 75, and low is Mg # < 50.
[c]Mg range based on the 2 μm band position: high is defined as roughly Mg # > 75, med ranges from Mg # 50 to 75, and low is Mg # < 50.

primarily in (1) the South Pole–Aitken (SPA) Basin and (2) the highlands north of Mare Imbrium and Mare Frigoris. The regions focused on for this paper are indicated by red boxes in Figure 1. The third box indicates the location of the crater Bullialdus, which has previously been recognized to have excavated low-Ca pyroxene-rich material [e.g., *Pieters*, 1991; *Tompkins et al.*, 1994]. All craters selected for compositional analyses are listed in Table 1.

4.2. Localized and Regional Concentrations of Low-Ca Pyroxene

4.2.1. Bullialdus Crater

[27] The M^3 coverage of Bullialdus during optical periods 1b and 2a is shown in Figure 2a. As has been previously noted, it is only the central peak that is dominated by a strong low-Ca pyroxene signature [e.g., *Pieters*, 1991; *Tompkins et al.*, 1994, *Cahill and Lucey*, 2007]; the remainder of the crater is more gabbroic. This is clearly seen in the LCP index map for the Bullialdus region, in which the central peak stands out prominently, but the surrounding region is almost low Ca pyroxene free (Figure 2b). The regions with the highest LCP index (0.15) correspond very well with the locations identified as norite and anorthositic norite dominated by *Cahill and Lucey* [2007].

[28] Shown in Figure 3 are spectra from the northwestern portion of the central peak of Bullialdus, centered at −20.7°, 337.5°. The spectra were extracted from approximately the same geographic region (within a single 140 m pixel of one another) in optical period 1b and optical period 2a data. These spectra represent moderately strong detections (LCP indices ~0.1) because due to the steep slopes on the central peak, the strongest detections from one optical period lie in shadow in the other. The data processed to apparent reflectance (ARFL) are shown as solid lines. For comparison, we also show the same spectra processed using the photometric model of *Hicks et al.* [2011] (PRFL, shown as dashed lines), which uses a Lommel-Seeliger correction instead of simply the cosine of the incidence angle. Also shown are straight-line continua drawn tangent to each spectrum from the bands at 1329 nm to 2457 nm. The continuum-removed spectra are shown in

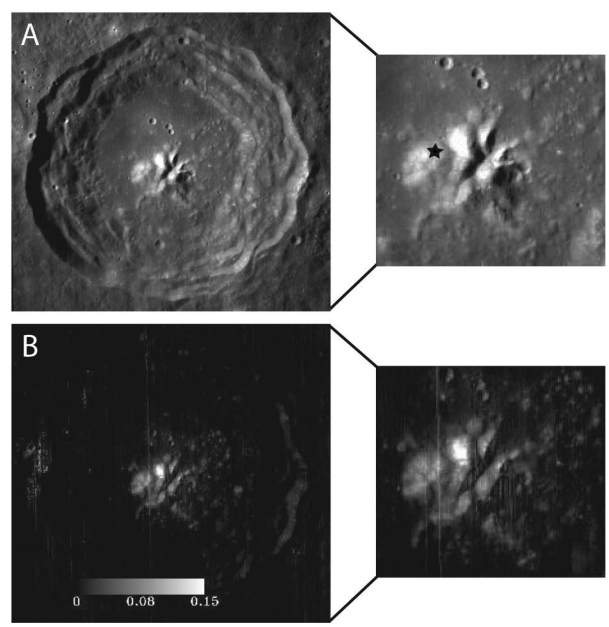

Figure 2. (a) Bullialdus crater as observed during optical period 2a. The star denotes the location from which the spectra were extracted for comparison between optical periods 1b and 2a. The brightest portion of the peak could not be used for comparison since it was in shadow during optical period 1b. (b) LCP index for Bullialdus. Only the central peak registers as having a strong low-Ca pyroxene signature: the gabbroic floor of the crater registers no detection for the LCP index parameter. Spatial resolution of the image is ~140 m/pixel.

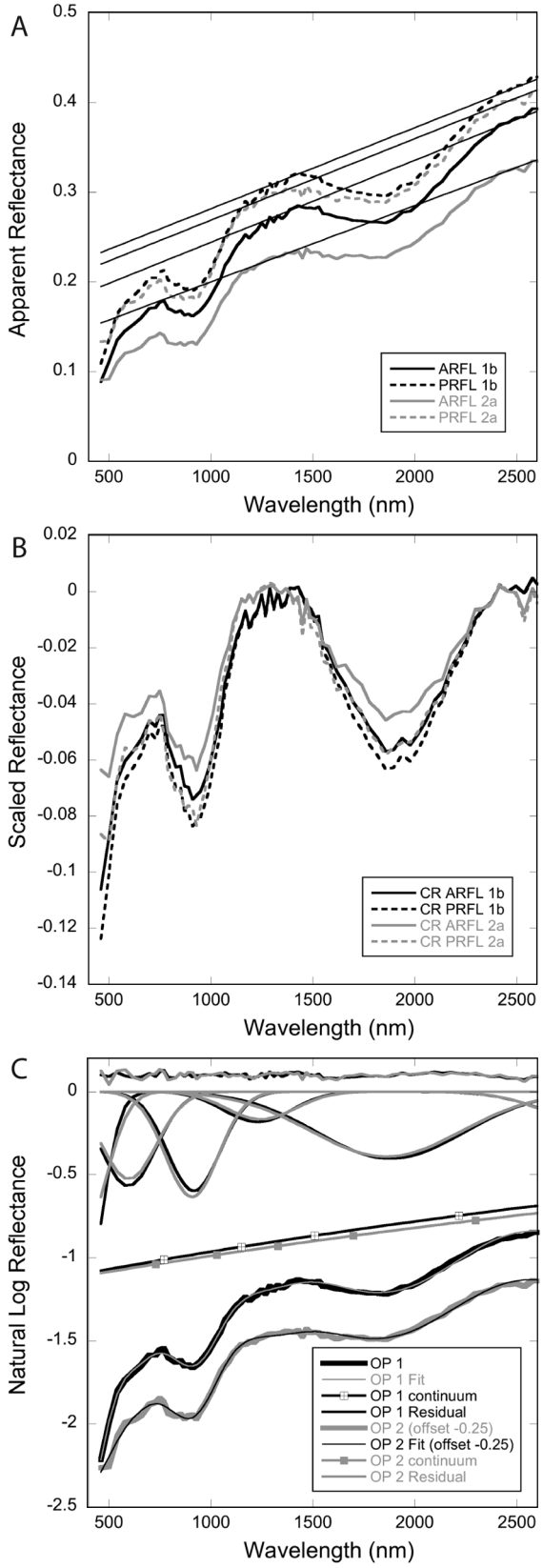

Figure 3. (a) Spectra extracted from Bullialdus crater for optical periods 1b and 2a, processed to apparent reflectance (ARFL) and photometrically corrected apparent reflectance (PRFL). (b) Straight-line continuum removed versions of the spectra shown in Figure 3a. Despite the initial difference in overall apparent reflectance, the band positions for the continuum-removed spectra are consistent. (c) MGM fits to the optical period 1b and 2a spectra for the same location. Optical period 1b data are shown as a thick black line. The continuum, deconvolved bands, and residual error also in black above the data. The fit line is shown in gray, superimposed on the data. Optical period 2a data are shown as a thick gray line, with the continuum, bands, and residual in gray and the fit in a thin black line on the data.

Figure 3b. The less steeply sloped data from optical period 2a appears to have a slightly shorter wavelength 1 μm and 2 μm band center. The difference is small, suggesting that there is good repeatability between optical periods and with different viewing geometries.

[29] Results of MGM fits for all spectra of the central peak of Bullialdus suggest that the 1 μm band is centered between 910 and 920 nm and the 2 μm band is centered between 1850 and 1880 nm, consistent with a relatively high Mg # (Mg # > 75). As illustrated in Figure 3c, the fits for both optical periods results in major absorption bands that are consistent to within at least 10 nm. The wavelength range of 910–920 nm is slightly shorter than reported for telescopic measurements of Bullialdus, which suggested a 1 μm band center near 930 nm [*Pieters*, 1991]. This difference is not surprising, since mixing of the gabbroic material surrounding the central peak in the larger field of view of the telescopic measurements (~10 km) would result in longer-wavelength pyroxene bands on average.

4.2.2. South Pole–Aitken Basin

[30] One of the most prominent regional concentrations of noritic material is in the South Pole–Aitken (SPA) Basin. Figure 4a is an enlarged map of the strongest low-Ca pyroxene detections, with numbers indicating the locations chosen for compositional modeling. The low-Ca pyroxene index is shown in red but is only obvious for the large exposures of low-Ca pyroxene. We have selected spectra from large and small exposures across the region in order to obtain a greater geographical diversity. Thus, many of the numbers are associated with small, fresh craters that are not obvious in this regional view. Noritic materials are associated with many of the large craters in the region and are readily observed along the walls, on central peaks or in fresh craters on the floors of the larger craters.

[31] Examples of two low-Ca pyroxene detections in SPA are shown in Figure 5. A small crater on the floor of Minkoswki crater (Figure 5a) exhibits relatively long 1 and 2 μm wavelength bands (Figure 5c). The MGM-derived band centers are consistent with a medium Mg # (Figure 5d). In general, the modeled band positions for the 2 μm band suggest higher iron contents than do those for the 1 μm band. Despite the global mode M^3 data having a coarser (40 nm) spectral sampling near 2 μm, the larger natural variation in 2 μm band position between a high- and low-iron orthopyroxene makes this spectral region more reliable for estimating

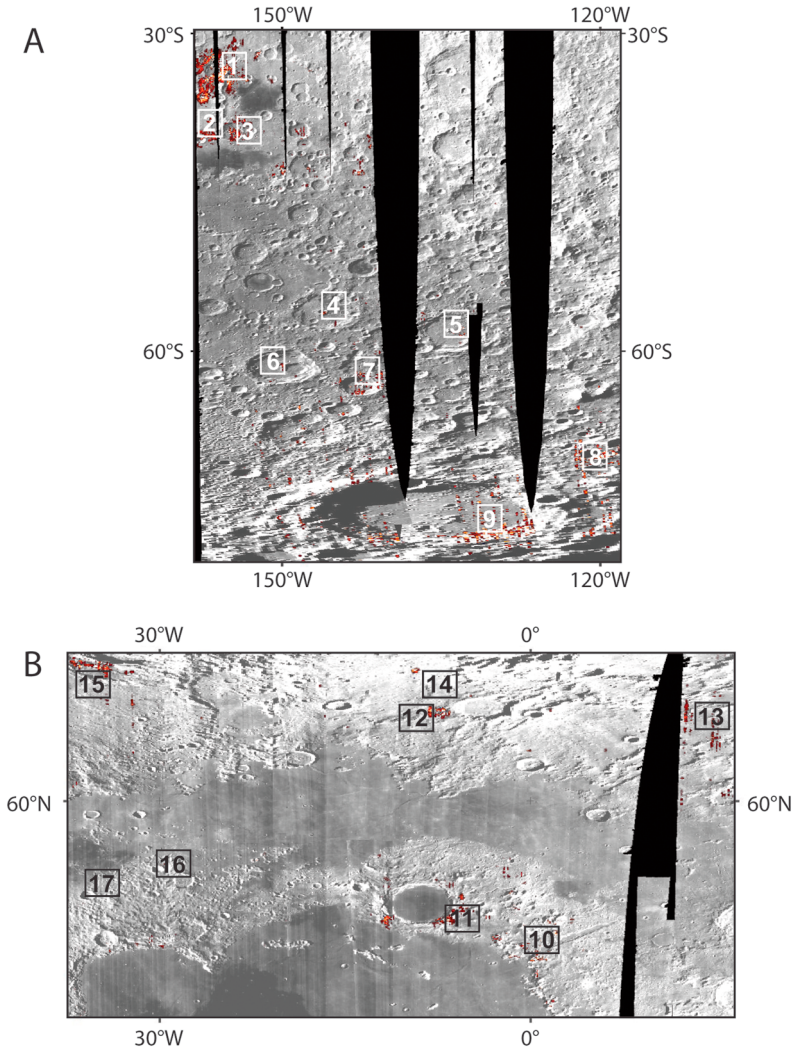

Figure 4. (a) Close-up view of the low-Ca pyroxene exposures in SPA with the sites selected for MGM modeling marked. Details for the sites are given in Table 1. (b) Close-up view of the low-Ca pyroxene exposures north and south of Mare Frigoris and their site numbers. LCP index is overlain in red, but several of the numbered sites are extracted from fresh craters beneath the scale of these images. Image resolution is ~1.4 km/pixel (10 × 10 binned global mode data).

pyroxene composition, particularly at high latitudes where the surface should be generally cooler.

[32] Though models of most SPA spectra suggest low-Ca pyroxenes with medium or low Mg #, Dryden (Figure 5b) and Chaffee S craters suggest higher Mg # content (Mg # > 75). Both craters are located along the inner ring of the Apollo Basin. As can be seen from Figure 5c, however, the band depths of the spectrum from Dryden crater are significantly weaker than some of the more iron-rich craters, resulting greater uncertainty in the spectral fits.

4.2.3. North Imbrium Norites

[33] An anomalous concentration of noritic material on the northern nearside of the Moon was noted in Clementine data [*Pieters*, 2002; *Isaacson and Pieters*, 2009]. This material is evident also in M^3 data, and includes some of the most prominent outcrops of low-Ca pyroxene-rich material detected in this study. Low-Ca pyroxene detections also occur south of Mare Frigoris along the northern border of Mare Imbrium, outside of the range of the northern Imbrium noritic anomaly [*Isaacson and Pieters*, 2009].

[34] As in the case of SPA, many of the exposures of low-Ca pyroxene in the highlands north and south of Mare Frigoris are within smaller craters. One prominent detection of low-Ca pyroxene occurs along the northern wall of Vallis Alpes (site 10 in Figure 3b). Low-Ca pyroxenes identified 'north of Mare Frigoris' (sites 12–15 in Figure 3b) and those identified in the ridge of highlands 'south of Mare Frigoris' (sites 10, 11, 16, 17) exhibit distinctive 1 and 2 μm band positions, suggesting different compositions in each region. Example spectra from both regions are shown in Figure 6. MGM-derived band positions (Figure 6d) from north of Mare Frigoris suggest dominantly medium Mg # low-Ca pyroxene, while those south of Mare Frigoris around the rim of Mare Imbrium consistently suggest more Mg #-rich pyroxene.

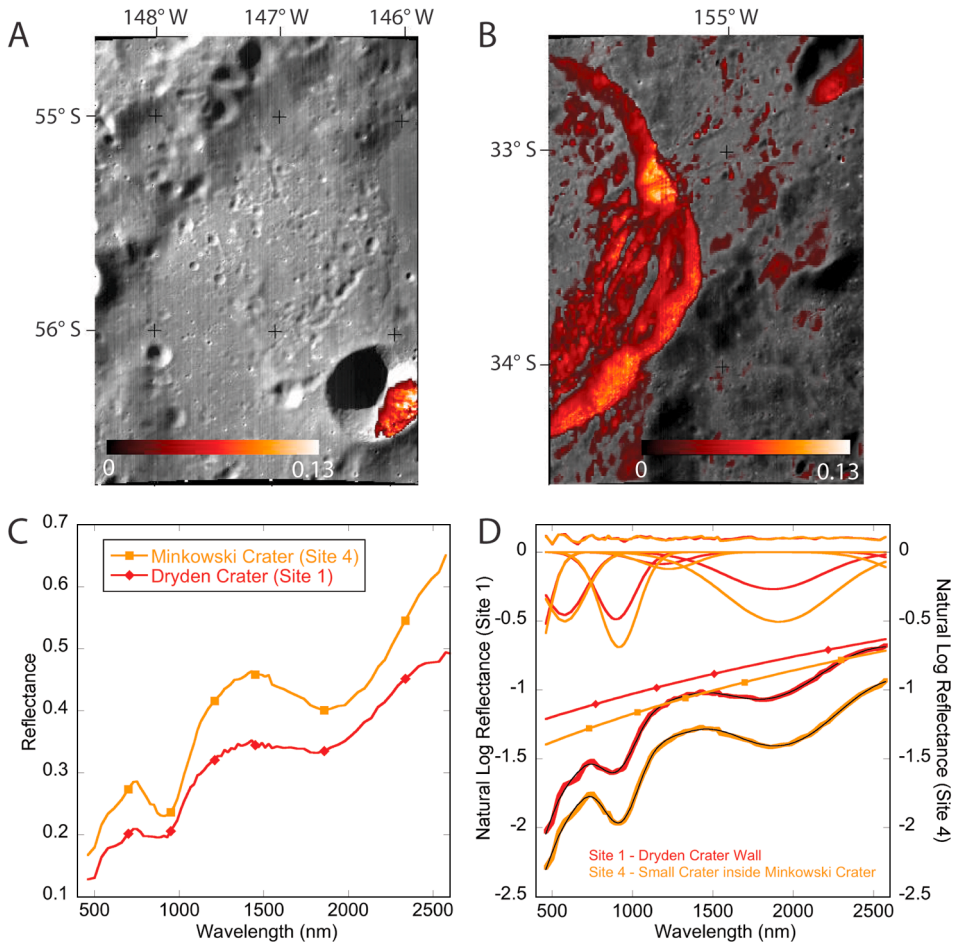

Figure 5. Examples of two sites from SPA. Base maps in Figures 5a and 5b are 750 nm albedo images at 140 m/pixel resolution. Red temperature color ramps are overlain, showing the LCP index for the region. (a) A small (~13 km diameter) crater in the floor of Minkowski crater. (b) Dryden crater. (c) Spectra from Minkowski and Dryden craters. The spectrum from Minkowski crater was extracted from the wall of the fresh crater depicted in Figure 5a, and the spectrum from Dryden crater was extracted from the high LCP index region on the inside of the crater wall at about 33.2°S. (d) MGM fits to Minkowski and Dryden crater spectra. Data, deconvolved bands, continuum, and residual are shown in orange for Minkowski crater and red for Dryden crater. Fits to each spectrum are superimposed on the data as thin black lines. The 1 and 2 μm bands in the spectrum of Dryden crater occur at shorter wavelengths than in Minkowski crater, suggesting that it has a moderately higher Mg #.

4.3. Global Compositional Trends

[35] Average derived band centers for the 20 modeled low-Ca pyroxene detections plot within the range of 1 and 2 μm band centers expected for orthopyroxene, as illustrated in Figure 7. The series of synthetic orthopyroxenes from *Klima et al.* [2007] ranges in composition from Mg_0 to $Mg_{97.5}$. Taking error bars into consideration, all of the 1 and 2 μm band centers are consistent with previous pyroxene studies (i.e., none have a 1 μm band that is significantly longer wavelength than would be expected based on the known relationship between 1 and 2 μm bands in pyroxene (Figure 7b)).

5. Implications

[36] Just over half of the pyroxenes examined in this work are modeled to be of moderate Mg #, consistent with orthopyroxenes found in association with the FAN suite (though pyroxenes of these compositions can also be found within the Mg suite). However, it is important to recognize that we have made our comparisons with Ca-free orthopyroxenes, which exhibit the shortest 1 and 2 μm bands of the pyroxene mineral suite. We have looked for regions devoid of mafics other than low-Ca pyroxene, but if either olivine or clinopyroxenes are also present at any site the 1 μm, and, for clinopyroxene, the 2 μm bands would occur at longer wavelengths than expected for pure orthopyroxene, giving the appearance of a higher iron content in the region. If significant olivine were present in any of these exposures, the 1 μm band would occur at a longer relative wavelength that expected based on the 2 μm band, which is not the case in any of the areas we focused on. Since the addition of Ca-rich pyroxene would result in longer wavelength 1 and 2 μm bands, our estimates should be considered closer to the lower limits of Mg # for these exposures.

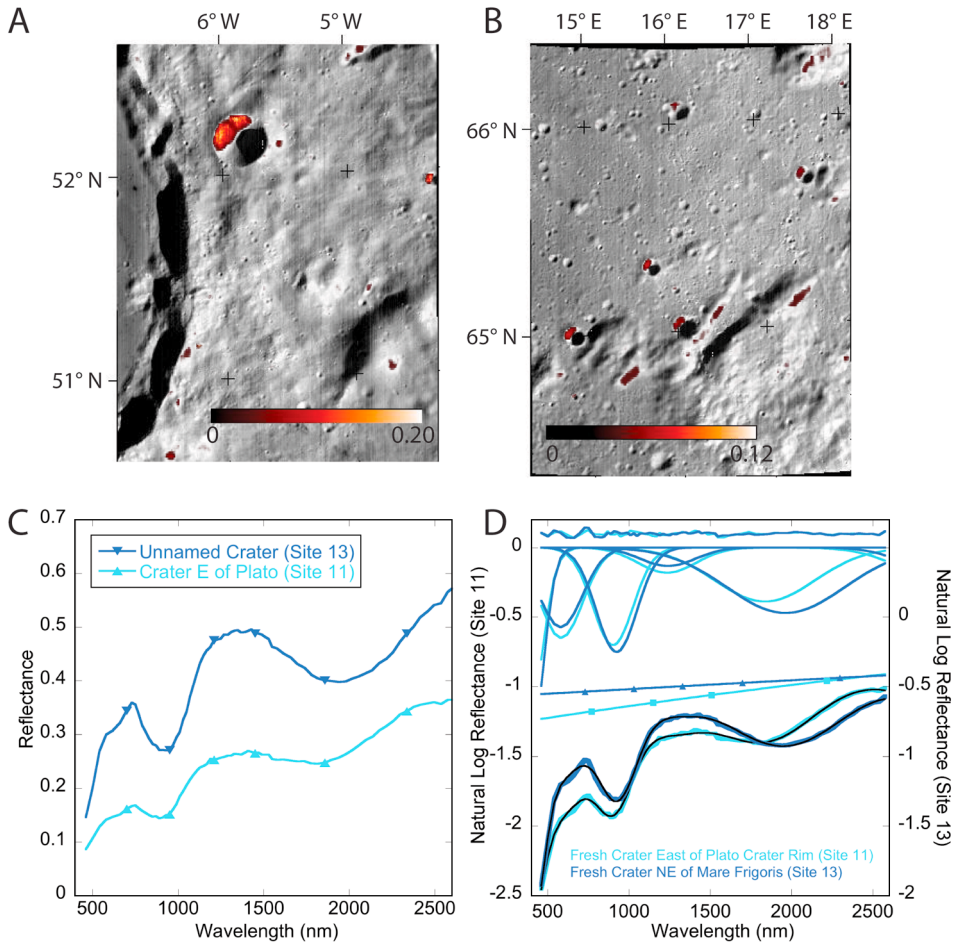

Figure 6. Examples of two sites from north and south of Mare Frigoris. Base maps in Figures 6a and 6b are 750 nm albedo images at 140 m/pixel resolution. Red temperature color ramps are overlain, showing the LCP index for the regions. (a) A small crater just east of the rim of Plato crater. (b) An unnamed fresh crater located near 65.3°N, 16°E, in the highlands north of Mare Frigoris. (c) Spectra from the craters in Figures 6a and 6b. (d) MGM fits to the spectra of the craters in Figures 6a and 6b. Data, deconvolved bands, continuum, and residual are shown in light blue for site 11 (Figure 6a) and dark blue for site 13 (Figure 6b). Fits to each spectrum are superimposed on the data as thin black lines. Both the 1 and 2 μm bands clearly occur at longer wavelengths in site 13 than in site 11.

[37] The strength of the pyroxene bands within craters in SPA and in the highlands north and south of Mare Frigoris suggest a higher concentration of pyroxene compared to that in a typical noritic anorthosite from the FAN suite. Our modeling suggests that the low-Ca pyroxenes north of Mare Frigoris and those in SPA are of moderate Mg # content, consistent with estimates of *Matsunaga et al.* [2008] based on Spectral Profiler measurements of the central peak of the SPA crater Antoniadi. The compositions of the northernmost low-Ca pyroxene detections span a similar compositional range to those in SPA, supporting the conclusion of *Isaacson and Pieters* [2009] that these are blanketing deposits of distal SPA ejecta (Figure 7). The northern Imbrium deposits are likely to represent mafic to ultramafic ejecta from the SPA event, sourced in the lower crust or upper mantle. At this stage, we cannot compositionally distinguish whether the exposures in SPA represent original material from the SPA impact or exposures of an ultramafic melt sheet created by it [*Morrison*, 1998; *Nakamura et al.*, 2009]. However, because most of the strong low-Ca pyroxene exposures detected here are not from the central peaks of craters within SPA, but rather from smaller, fresh craters within surficial deposits, sampling of a melt sheet is more likely. In either case, the majority of low-Ca pyroxenes exposed in SPA are not significantly enriched in Mg #, suggesting that they are not tapping Mg suite intrusions and that the material excavated by the SPA impact was relatively iron rich.

[38] The initial compositional modeling results presented here support the hypothesis of *Petro et al.* [2010] that the Apollo Basin tapped of a different composition material than did other smaller impacts into the SPA melt sheet. The 480 km diameter, pre-Nectarian Apollo basin is located on the edge of SPA, and sits above some of the thinnest crust on the Moon [*Ishihara et al.*, 2009; *Petro et al.*, 2010]. We modeled three low-Ca pyroxenes from around the Apollo Basin (sites 1–3 in Figure 3a). Two of these spectra, Dryden (site 1) and Chaffee S (site 2) craters suggest more Mg-rich spectral signatures than the rest of SPA (Figure 7). The

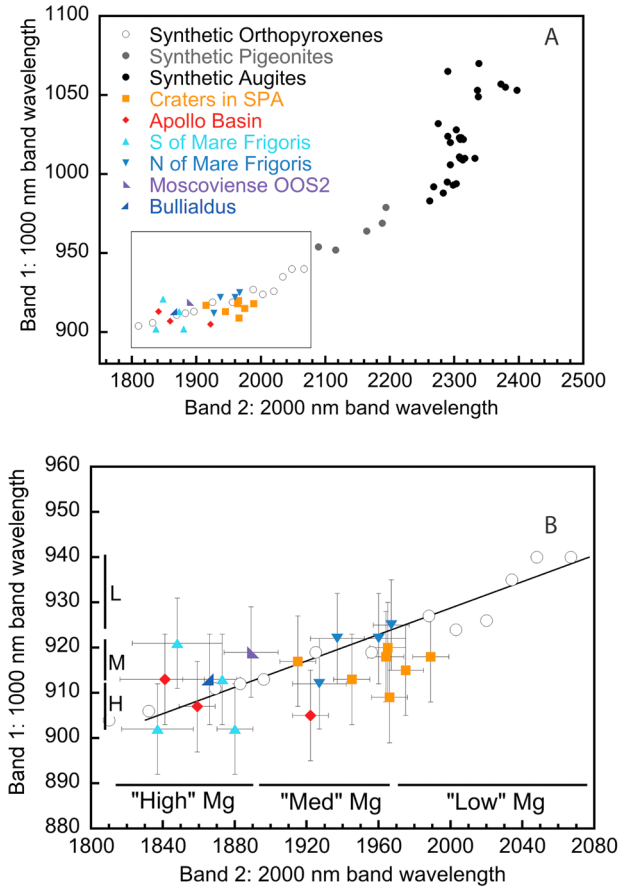

Figure 7. (a) Comparison of the 1 and 2 μm band positions for all 20 low-Ca pyroxene exposures modeled herein with the synthetic pyroxenes measured by *Klima et al.* [2007, 2011]. Error bars have been omitted to avoid excessive clutter. (b) Closer view of the band position of the low-Ca pyroxene exposures (boxed area from Figure 7a with error bars included. The wavelength ranges for the 1 and 2 μm bands that correspond with high (H), medium (M) and low (L) Mg # for the synthetic orthopyroxenes are indicated.

spectrum of Dryden crater was extracted from along the eastern wall of Dryden crater, closest to the inner ring of Apollo, and Chaffee S also lies near the inner ring. There are several possibilities to explain the more magnesian character of these low-Ca pyroxenes. Given the thin nature of the crust at Apollo, and the positioning of the high Mg # detections on the inner ring of the basin, it is possible that Apollo excavated deeper primary crustal (or mantle) material than is exposed elsewhere in SPA. It is also possible that, if SPA is covered by a differentiated melt sheet, the Apollo Basin excavated material from a more magnesian cumulate pile at its base. Finally, it is possible that Apollo impacted a local Mg-rich intrusion, possibly emplaced after the SPA-forming impact. Further geologic mapping and detailed compositional analysis of the Apollo Basin are required to better constrain the origin of these anomalous materials.

[39] The low-Ca pyroxenes located south of Mare Frigoris, in the highlands just north of Mare Imbrium, were also found to be high in Mg #. The modeled spectra (sites 10, 11, 16, 17) exhibit strong noritic signatures, and the 1 and 2 μm bands occur at short wavelengths, bands consistent with high Mg # (Mg # > 80–90). Given the coincidence of these low-Ca, high Mg # pyroxenes with a thorium signature measured by Lunar Prospector (Figure 4b), they are very good candidates for KREEP-related Mg suite pyroxenes. Interestingly, several of the locations (particularly near Vallis Alpes, site 10) are close to the olivine exposures found by the Spectral Profiler on Kaguya around the Imbrium Basin [*Yamamoto et al.*, 2010]. With detailed mapping, the stratigraphical relationship between the olivine and low-Ca pyroxene exposures may provide additional constraints on whether these are troctolitic and noritic Mg suite intrusions or plausibly lower crustal and/or mantle material.

[40] In addition to the broader regional exposures of low-Ca pyroxenes, we modeled spectra from a northern portion of the central peak of Bullialdus (Figure 2) and from a low-Ca pyroxene found in association with spinel on the inner ring of the Moscoviense basin (OOS2 by *Pieters et al.* [2011]). Bullialdus, located within the PKT, appears to have a relatively high Mg # (Figure 7). Given the regionally isolated nature of the low-Ca pyroxenes detected at Bullialdus, it is another strong candidate for an Mg suite pluton. The exposure at Moscoviense, described in detail by *Pieters et al.* [2011], appears to be slightly more iron rich, plotting near the boundary between high and medium Mg # pyroxenes. Moscoviense lies above the thinnest crust on the Moon [*Ishihara et al.*, 2009], suggesting that these exposures may sample the lower crust [*Pieters et al.*, 2011].

[41] All of the exposures modeled in this work are located in or near the regions predicted to be Mg suite like on the basis of radiative transfer modeling of Clementine data [*Lucey and Cahill*, 2009]. Since we have focused only on the compositions of the pyroxenes themselves, we cannot directly address the bulk compositions of the rocks at each site. It is encouraging that modal mineralogy estimated from Clementine is consistent with Mg suite rocks in the areas where we have identified candidate Mg suite compositions. Though we have concluded that over half of the modeled exposures are consistent with FAN pyroxene composition, it is also possible that these are pyroxenes crystallized in later stage intrusions with higher iron content Mg suite or Mg suite-like bulk compositions.

6. Conclusions and Future Work

[42] In an initial survey of M^3 data, regional exposures of strong low-Ca pyroxene signatures are predominantly found within SPA and in the highlands north and south of Mare Frigoris (Figures 1 and 4). Approximately half of the pyroxenes are modeled to have moderate Mg # content, and are most consistent with compositions found in association with typical FAN rocks. A few localities, however, do appear to have high Mg # values (Mg # > 75). Several exposures along the inner ring of the Apollo Basin tap a higher Mg# source than the majority of SPA craters modeled here. Low-Ca pyroxene deposits south of Mare Frigoris and around the Imbrium Basin are also found have high Mg # spectral signatures. In particular, the low-Ca pyroxenes around Mare Imbrium are currently good candidates for exposure of Mg suite intrusions or lower crustal material. In the next steps of our analysis of M^3 data, thermal and photometric corrections using high-resolution Lunar Orbiter Laser Altimeter (LOLA)

or Lunar Reconnaissance Orbiter Camera digital elevation model topography data will permit even more specific estimations of the composition of pyroxene outcrops, as well as more detailed mapping of the geologic context of the exposures. These further calibrated data will be suitable for radiative transfer modeling of the spectra, enabling the relative proportions of pyroxene and plagioclase to be constrained and compared with the Mg # maps of *Lucey and Cahill* [2009].

[43] **Acknowledgments.** We are grateful to Joshua Cahill for a thorough and helpful review that greatly improved our manuscript. The M^3 instrument was funded as a mission of opportunity through the NASA Discovery program. M^3 science validation is supported through NASA contract NNM05AB26C. Partial funding for this analysis has also been provided through NASA LSI at the Applied Physics Lab under contract NNA09DB31A. We are extremely grateful to ISRO for the opportunity to fly as a guest instrument on Chandrayaan-1. The views, opinions, and/or findings contained in this paper are those of the authors and should not be interpreted as representing the official views, either expressed or implied, of the Defense Advanced Research Projects Agency or the Department of Defense.

References

Adams, J. B. (1974), Visible and near-infrared diffuse reflectance spectra of pyroxenes as applied to remote sensing of solid objects in the solar system, *J. Geophys. Res.*, *79*, 4829–4836, doi:10.1029/JB079i032p04829.

Boardman, J. W., C. M. Pieters, R. O. Green, S. Lundeen, P. Varansi, J. Nettles, N. E. Petro, P. J. Isaacson, S. Besse, and L. A. Taylor (2011), Measuring moonlight: An overview of the spatial properties, lunar coverage, selenolocation and related level 1B products of the Moon Mineralogy Mapper, *J. Geophys. Res.*, doi:10.1029/2010JE003730, in press.

Burns, R. G. (1993), *Mineralogical Applications of Crystal Field Theory*, Cambridge Univ. Press, Cambridge, U. K., doi:10.1017/CBO9780511524899.

Cahill, J. T., and P. G. Lucey (2007), Radiative transfer modeling of lunar highlands spectral classes and relationship to lunar samples, *J. Geophys. Res.*, *112*, E10007, doi:10.1029/2006JE002868.

Cahill, J. T., P. G. Lucey, and M. A. Wieczorek (2009), Compositional variations of the lunar crust: Results from radiative transfer modeling of central peak spectra, *J. Geophys. Res.*, *114*, E09001, doi:10.1029/2008JE003282.

Clark, R. N., C. M. Pieters, R. O. Green, J. W. Boardman, and N. E. Petro (2011), Thermal removal from near-infrared imaging spectroscopy data of the Moon, *J. Geophys. Res.*, doi:10.1029/2010JE003751, in press.

Cloutis, E. A., and M. J. Gaffey (1991), Pyroxene spectroscopy revisited: Spectral-compositional correlations and relationship to geothermometry, *J. Geophys. Res.*, *96*, 22,809–22,826, doi:10.1029/91JE02512.

Cloutis, E. A., R. L. Klima, L. Kaletzke, A. Coradini, L. A. McFadden, D. I. Shestopalov, and F. Vilas (2010), The 506 nm absorption feature in pyroxene spectra: Nature and implications for spectroscopy-based studies of pyroxene-bearing targets, *Icarus*, *207*, 295–313, doi:10.1016/j.icarus.2009.11.025.

Denevi, B. W., P. G. Lucey, E. J. Hochberg, and D. Steutel (2007), Near-infrared optical constants of pyroxene as a function of iron and calcium content, *J. Geophys. Res.*, *112*, E05009, doi:10.1029/2006JE002802.

Goswami, J. N., and M. Annadurai (2009), Chandrayaan-1: India's first planetary science mission to the Moon, *Lunar Planet. Sci. [CD-ROM]*, *40*, Abstract 2571.

Heiken, G. H., D. T. Vaniman, and B. M. French (1991), *Lunar Sourcebook: A User's Guide to the Moon*, Cambridge Univ. Press, New York.

Hess, P. C., and E. M. Parmentier (1995), A model for the thermal and chemical evolution of the Moon's interior: Implications for the onset of mare volcanism, *Earth Planet. Sci. Lett.*, *134*, 501–514, doi:10.1016/0012-821X(95)00138-3.

Hicks, M. D., B. J. Buratti, J. Nettles, M. Staid, J. Sunshine, C. M. Pieters, S. Besse, and J. Boardman (2011), A photometric function for analysis of lunar images in the visual and infrared based on Moon Mineralogy Mapper observations, *J. Geophys. Res.*, doi:10.1029/2010JE003733, in press.

Hiroi, T., C. M. Pieters, and S. K. Noble (2000), *Lunar Planet. Sci. [CD-ROM]*, *31*, Abstract 1548.

Isaacson, P. J., and C. M. Pieters (2009), Northern Imbrium Noritic anomaly, *J. Geophys. Res.*, *114*, E09007, doi:10.1029/2008JE003293.

Ishihara, Y., S. Goossens, K. Matsumoto, H. Noda, H. Araki, N. Namiki, H. Hanada, T. Iwata, S. Tazawa, and S. Sasaki (2009), Crustal thickness of the Moon: Implications for farside basin structures, *Geophys. Res. Lett.*, *36*, L19202, doi:10.1029/2009GL039708.

Jolliff, B. L., J. J. Gillis, L. A. Haskin, R. L. Korotev, and M. A. Wieczorek (2000), Major lunar crustal terranes: Surface expressions and crust-mantle origins, *J. Geophys. Res.*, *105*, 4197–4216, doi:10.1029/1999JE001103.

Kanner, L. C., J. F. Mustard, and A. Gendrin (2007), Assessing the limits of the Modified Gaussian Model for remote spectroscopic studies of pyroxenes on Mars, *Icarus*, *187*, 442–456, doi:10.1016/j.icarus.2006.10.025.

Klima, R. L., C. M. Pieters, and M. D. Dyar (2007), Spectroscopy of synthetic Mg-Fe pyroxenes I: Spin-allowed and spin-forbidden crystal field bands in the visible and near-infrared, *Meteorit. Planet. Sci.*, *42*, 235–253, doi:10.1111/j.1945-5100.2007.tb00230.x.

Klima, R. L., C. M. Pieters, and M. D. Dyar (2008), Characterization of the 1.2 μm M1 pyroxene band: Extracting cooling history from near-IR spectra of pyroxenes and pyroxene-dominated rocks, *Meteorit. Planet. Sci.*, *43*, 1591–1604, doi:10.1111/j.1945-5100.2008.tb00631.x.

Klima, R. L., C. M. Pieters, and M. D. Dyar (2009), Pyroxene spectroscopy: Probing composition and thermal history of the lunar surface, *Lunar Planet. Sci. [CD-ROM]*, *40*, Abstract 2155.

Klima, R. L., M. D. Dyar, and C. M. Pieters (2011), Near-infrared spectra of clinopyroxenes: Effects of calcium content and crystal structure, *Meteorit. Planet. Sci.*, *46*, 379–395, doi:10.1111/j.1945-5100.2010.01158.x.

Lindsley, D. H. (1983), Pyroxene thermometry, *Am. Mineral.*, *68*, 477–493.

Lucey, P. G., and J. T. Cahill (2009), The composition of the lunar surface relative to samples, *Lunar Planet. Sci. [CD-ROM]*, *40*, Abstract 2424.

Matsunaga, T., et al. (2008), Discoveries on the lithology of lunar crater central peaks by SELENE spectral profiler, *Geophys. Res. Lett.*, *35*, L23201, doi:10.1029/2008GL035868.

Morrison, D. A. (1998), Did a thick South Pole–Aitken Basin melt sheet differentiate to form cumulates?, *Lunar Planet. Sci. [CD-ROM]*, *29*, Abstract 1657.

Mustard, J. F., et al. (2011), Compositional diversity and geologic insights of the Aristarchus crater from Moon Mineralogy Mapper data, *J. Geophys. Res.*, doi:10.1029/2010JE003726, in press.

Nakamura, R., et al. (2009), Ultramafic impact melt sheet beneath the South Pole–Aitken Basin on the Moon, *Geophys. Res. Lett.*, *36*, L22202, doi:10.1029/2009GL040765.

Noble, S. K., C. M. Pieters, T. Hiroi, and L. A. Taylor (2006), Using the modified Gaussian model to extract quantitative data from lunar soils, *J. Geophys. Res.*, *111*, E11009, doi:10.1029/2006JE002721.

Petro, N. E., J. Sunshine, C. Pieters, R. Klima, J. Boardman, S. Besse, J. Head, P. Isaacson, L. Taylor, and S. Tompkins (2010), Lower crustal materials exposed in the Apollo basin revealed using Moon Mineralogy Mapper (M^3) data, *Lunar Planet. Sci. [CD-ROM]*, *41*, Abstract 1802.

Pieters, C. M. (1991), Bullialdus: Strengthening the case for lunar plutons, *Geophys. Res. Lett.*, *18*(11), 2129–2132, doi:10.1029/91GL02668.

Pieters, C. M. (2002), Give and take between SPA and Imbrium basins, *Lunar Planet. Sci. [CD-ROM]*, *33*, Abstract 1776.

Pieters, C. M., et al. (2009), Character and spatial distribution of OH/H_2O on the surface of the Moon seen by M^3 on Chandrayaan-1, *Science*, *326*, 568–572, doi:10.1126/science.1178658.

Pieters, C. M., et al. (2011), Mg-spinel lithology: A new rock-type on the lunar farside, *J. Geophys. Res.*, doi:10.1029/2010JE003727, in press.

Ryder, G. (1991), Lunar ferroan anorthosites and mare basalt sources: The mixed connection, *Geophys. Res. Lett.*, *18*(11), 2065–2068, doi:10.1029/91GL02535.

Ryder, G., and J. A. Wood (1977), Serenitatis and Imbrium impact melts: Implications for large-scale layering in the lunar crust, *Proc. Lunar Planet. Sci. Conf.*, *8*, 655–668.

Saxena, S. K., and S. Ghose (1971), Mg^{2+}-Fe^{2+} order-disorder and the thermodynamics of the orthopyroxene crystalline solution, *Am. Mineral.*, *56*, 532–559.

Shearer, C. K., and J. Papike (2005), Early crustal building processes on the moon: Models for the petrogenesis of the magnesian suite, *Geochim. Cosmochim. Acta*, *69*, 3445–3461, doi:10.1016/j.gca.2005.02.025.

Shearer, C. K., et al. (2006), Thermal and magmatic evolution of the Moon, in *New Views of the Moon*, *Rev. Mineral. Geochem.*, vol. 60, edited by B. L. Jolliff et al., pp. 365–518, Mineral. Soc. of Am., Chantilly, Va., doi:10.2138/rmg.2006.60.4.

Sunshine, J. M., and C. M. Pieters (1993), Estimating modal abundances from the spectra of natural and laboratory Pyroxene mixtures using the modified Gaussian model, *J. Geophys. Res.*, *98*, 9075–9087, doi:10.1029/93JE00677.

Sunshine, J. M., C. M. Pieters, and S. F. Pratt (1990), Deconvolution of mineral absorption bands: An improved approach, *J. Geophys. Res.*, *95*, 6955–6966, doi:10.1029/JB095iB05p06955.

Sunshine, J. M., C. M. Pieters, S. F. Pratt, and K. S. McNaron-Brown (1999), Absorption band modeling in reflectance spectra: Availability of the modified Gaussian model, *Lunar Planet. Sci. [CD-ROM]*, *30*, Abstract 1306.

Tompkins, S., and C. M. Pieters (1999), Mineralogy of the lunar crust: Results from Clementine, *Meteorit. Planet. Sci.*, *34*, 25–41, doi:10.1111/j.1945-5100.1999.tb01729.x.

Tompkins, S., C. M. Pieters, J. F. Mustard, P. Pinet, and S. D. Chevrel (1994), Distribution of materials excavated by the lunar crater Bullialdus and implications for the geologic history of the Nubium region, *Icarus*, *110*, 261–271, doi:10.1006/icar.1994.1120.

Virgo, D., and S. S. Hafner (1970), Fe^{2+}, Mg order-disorder in natural orthopyroxenes, *Am. Mineral.*, *55*, 201–223.

Warren, P. H. (1985), The magma ocean concept and lunar evolution, *Annu. Rev. Earth Planet. Sci.*, *13*, 201–240, doi:10.1146/annurev.ea.13.050185.001221.

Warren, P. H. (1990), Lunar anorthosites and the magma-ocean plagioclase-flotation hypotheses: Importance of FeO enrichment in the parent magma, *Am. Mineral.*, *75*, 46–58.

Wieczorek, M. A., and R. J. Phillips (2000), The "Procellarum KREEP terrane": Implications for mare volcanism and lunar evolution, *J. Geophys. Res.*, *105*, 20,417–20,430, doi:10.1029/1999JE001092.

Wood, J. A., J. S. Dickey Jr., U. B. Marvin, and B. N. Powell (1970), Lunar anorthosites and a geophysical model for the Moon, *Proc. Apollo 11 Lunar Sci. Conf., Geochim. Cosmochim. Acta*, Suppl. 1, 965–988.

Yamamoto, S., et al. (2010), Possible mantle origin of olivine around lunar impact basins detected by SELENE, *Nat. Geosci.*, *3*, 533–536, doi:10.1038/ngeo897.

J. W. Boardman, Analytical Imaging and Geophysics LLC, 4450 Arapahoe Ave., Ste. 100, Boulder, CO 80305, USA.

R. O. Green, Jet Propulsion Laboratory, 4800 Oak Grove Dr., MS 306-438, Pasadena, CA 91109-8099, USA.

J. W. Head III, P. J. Isaacson, J. F. Mustard, J. W. Nettles, and C. M. Pieters, Department of Geological Sciences, Brown University, Box 1846, Providence, RI 02912, USA.

R. L. Klima, Johns Hopkins University Applied Physics Laboratory, 11100 Johns Hopkins Rd., Laurel, MD 20732-0000, USA. (rachel.klima@jhuapl.edu)

N. E. Petro, NASA Goddard Space Flight Center, Code 698, Greenbelt, MD 20771, USA.

M. Staid, Planetary Science Institute, 1700 E. Fort Lowell, Ste. 106, Tucson, AZ 85719, USA.

J. M. Sunshine, Department of Astronomy, University of Maryland, College Park, MD 20742-2421, USA.

L. A. Taylor, Planetary Geosciences Institute, Department of Earth and Planetary Sciences, University of Tennessee, 1412 Circle Dr., Knoxville, TN 37996-1410, USA.

S. Tompkins, Defense Advanced Research Projects Agency, 3701 N. Fairfax Dr., Arlington, VA 22203-1714, USA.